



1 Characterization of Non-Gaussianity in the Snow  
2 Distributions of Various Landscapes

3

4 **Noriaki Ohara<sup>1</sup>, Andrew D. Parsekian<sup>1</sup>, Benjamin M. Jones<sup>2</sup>, Rodrigo C. Rangel<sup>1</sup>, Kenneth**  
5 **M. Hinkel<sup>3</sup>, and Rui A. P. Perdigão<sup>4,5</sup>**

6 <sup>1</sup>University of Wyoming, Laramie, WY, USA

7 <sup>2</sup>University of Alaska Fairbanks, Fairbanks, AK, USA

8 <sup>3</sup>Michigan Technological University, Houghton, MI, USA

9 <sup>4</sup>Meteoceanics Institute for Complex System Science, IUC Physics of Complex Coevolutionary  
10 Systems & Fluid Dynamical Systems, Washington, DC, USA

11 <sup>5</sup>Synergistic Manifolds, Lisbon, Portugal

12

13 Corresponding author: Noriaki Ohara (nohara1@uwyo.edu)

14 **Summary**

15 Snow distribution characterization is essential for accurate snow water estimation for water  
16 resource prediction from existing in-situ observations and remote sensing data at a finite spatial  
17 resolution. Four different observed snow distribution datasets were analyzed for Gaussianity. It  
18 was found non-Gaussianity of snow distribution is a signature of wind redistribution effect.  
19 Generally, seasonal snowpack can be well approximated by Gaussian distribution for fully snow-  
20 covered area.



## 21 **Abstract**

22 Seasonal snowpack is an important predictor of available water resources in the following spring  
23 and early summer melt season. Total basin snow water equivalent (SWE) estimation usually  
24 requires a form of statistical analysis that is implicitly built upon the Gaussian framework.  
25 However, it is important to characterize the non-Gaussian properties of snow distribution for  
26 accurate large-scale SWE estimation based on remotely sensed or sparse ground-based  
27 observations. This study quantified non-Gaussianity using sample negentropy, the Kullback–  
28 Leibler divergence from Gaussian distribution, for field-observed snow depth data on the North  
29 Slope, Alaska, and three representative SWE distributions in the western US from the Airborne  
30 Snow Observatory (ASO). Snowdrifts around lakeshore cliffs and deep gullies can bring  
31 moderate non-Gaussianity in the open, lowland tundra of North Slope, Alaska, while the ASO  
32 dataset suggests that subalpine forests may effectively suppress the non-Gaussianity of snow  
33 distribution. Thus, non-Gaussianity is found in areas with partial snow cover and wind-induced  
34 snowdrifts around topographic breaks in slope and other steep terrain features. The snowpacks  
35 may be considered weakly Gaussian in coastal regions with open tundra in Alaska and alpine and  
36 subalpine terrains in the western US if the land is completely covered by snow. The wind-  
37 induced snowdrift effect can be potentially partitioned from the observed snow spatial  
38 distribution guided by its Gaussianity.

39

## 40 **1 Introduction**

41 Modeling of the spatial variability of snow is important for large-scale earth surface modeling  
42 since atmospheric circulation is sensitive to snow cover presence (e.g., Aas et al., 2016; Meng,  
43 2017; Mott et al., 2015, 2017; Nitta et al., 2014; Younas et al., 2017). Since subgrid variability  
44 often causes appreciable bias in weather predictions, accurate snow cover quantification can  
45 potentially improve the predictability of weather, planetary boundary-layer evolution, convective  
46 cloud formation, and even tropical cyclogenesis (Santanello et al., 2018). Hence, the subgrid  
47 variability of snow cover has been incorporated into operational regional weather forecasting  
48 models such as the High-Resolution Rapid Refresh (HRRR) model (He et al., 2021).

49 Observations of seasonal snow storage in mountainous areas through remote sensing and ground-  
50 based measurements are a direct and reliable indicator of the water supply during the following  
51 spring season in downstream regions (e.g. Fleming et al., 2023; Sengupta et al., 2022). However,  
52 total basin snow water equivalent (SWE) estimation usually requires a statistical relationship  
53 such as the snow depletion curve (SDC), which correlates with observables such as the snow  
54 cover area fraction (SCF). Based on a study of the observed snow distributions in Reynolds  
55 Creek Experimental Watershed in Idaho, Luce et al. (1999) showed that one snow distribution  
56 can reasonably represent the SDC evolution for the rest of the season. Also, Luce and Turboton  
57 (2004) showed a high degree of similarity in nine years of dimensionless depletion curves  
58 measured in the same basin. Shamir and Georgakakos (2007) demonstrated the consistency of  
59 SDC over a season in the American River using a distributed model. The subseasonal and



60 interseasonal consistency in SDCs suggests the possibility for subgrid snow characterization as  
61 well as SWE estimation from SCF data such as the MODIS product (Hall et al., 2006).

62 As remote sensing technologies advance, seasonal snow distribution characterization becomes  
63 more approachable with multi-sensor methods. For example, Tarricone et al. (2023) analyzed  
64 three Interferometric Synthetic Aperture Radar (InSAR) image pairs to assess SWE evolution  
65 using the snow-focused multi-sensor method with Uninhabited Aerial Vehicle Synthetic  
66 Aperture Radar (UAVSAR) and an L-band InSAR data as well as optical fractional snow-  
67 covered area (SCA) information. However, to estimate the total basin SWE in water resource  
68 management practices, statistical empirical relationships are required to fill gaps in the spatial  
69 and temporal resolutions—even when using these remote sensing observations (Tsang et al.,  
70 2022). For example, Meloche et al. (2022) assumed log-normal distribution to represent the sub-  
71 pixel variability of remotely sensed data. Thus, uncertainty and subgrid variability must be  
72 accounted for when using statistical characterization in SWE estimation.

73 The most popular choice for the probability density function (PDF) of snow is log-normal  
74 distribution, which inherently eliminates negative snow depth (Donald et al., 1995; Liston, 2004;  
75 and many others). Brubaker and Menoes (2001) chose a beta distribution, while Kolberg and  
76 Gottschalk (2006) selected a two-parameter  $\gamma$ -distribution. Although these common distributions  
77 are in the exponential family, they were primarily chosen for convenience. Indeed, the  
78 representativeness of these parametric probability distributions remains questionable for different  
79 landscapes and snowpack ages (e.g., Skaugen & Randen, 2013; Egli & Jonas, 2009; He, Ohara,  
80 & Miller, 2019). Moreover, these approaches for bounded distributions may not work for  
81 evolving snowpacks with partial SCA where zero values are present in the probability domain.

82 In theory, since the landing location of each snow particle fallen from the atmosphere is  
83 considered an independent and identically distributed (iid) random variable, the resulting snow  
84 depth or SWE distribution should asymptotically approach a Gaussian distribution due to the  
85 central limit theorem. He, Ohara, and Miller (2019) reported Gaussian snow distributions in  
86 many of the forested, fully snow-covered areas during the peak snow season using airborne Light  
87 Detection and Ranging (LiDAR) observations in the Snowy Range, Wyoming. This implies the  
88 presence of both systematic (non-Gaussian) and random (Gaussian) mechanisms in snow  
89 accumulation and ablation processes. Therefore, it is possible to identify the potential factors as  
90 “signals” that make the snow distribution deviate from a Gaussian distribution by analyzing the  
91 resultant snow distributions.

92 This study applies negentropy to analyze the non-Gaussianity of snow distributions in Arctic  
93 tundra, as well as alpine and subalpine landscapes in North America. Negentropy measures the  
94 departure in entropy between a sampled distribution and Gaussian distribution of identical  
95 variance and mean. Signals of interest (e.g., systematic snowdrift patterns) can be extracted as  
96 non-Gaussian components because pure random noise asymptotically becomes Gaussian in  
97 theory. This is the main idea of independent component analysis (ICA; Hyvärinen et al., 2000).  
98 This work presents the quantified non-Gaussianity of the observed snow distributions through a  
99 variety of snow distribution data, including intense direct hand measurements within 30-m grids  
100 using a probe, and indirect measurements using a snowmachine-attached ground-penetrating



101 radar (GPR), UAV-based photogrammetry, as well as the Airborne Snow Observatory (ASO)  
102 SWE products.

## 103 2 Methods

### 104 2.1 Negentropy

105 To measure the non-Gaussianity of any data, we implement the information-theoretic metric of  
106 negentropy as the objective function since negentropy is equal to the Kullback–Leibler  
107 divergence between  $p_x$  and a Gaussian distribution with the same mean and variance as  $p_x$ .  
108 There is a well-known proposition that Gaussian density has the largest information entropy  
109 among all unbounded distributions with the same first and second-order statistics. As such, the  
110 non-Gaussianity of an observed distribution can be quantified by negentropy  $J$ , which is defined  
111 as follows (Hyvärinen et al., 2000):

$$112 \quad J(X) = S(X_{gauss}) - S(X) \quad (1)$$

113 where  $S$  is the information entropy of  $X$ . The information entropy can assume a diversity of  
114 metrics ranging from the most general capturing microphysical event-scale codependence in  
115 nonlinear statistical mechanics (Perdigão 2018) or simply assuming basic event-scale  
116 independence in classical information theory (Shannon (1948) statistical entropy). For the  
117 purpose of this study, we take the latter simple form, which is defined as:

$$118 \quad S(X) = - \int p_x(\eta) \log[p_x(\eta)] d\eta. \quad (2)$$

119 The Edgeworth expansion (Edgeworth, 1905) can provide an approximation for a PDF of  $X$ , as  
120 follows:

$$121 \quad p_x(X) = \frac{\phi(U)}{\sigma} \left[ 1 + \frac{\kappa_3}{6} H_3(U) + \frac{\kappa_4}{24} H_4(U) + \frac{\kappa_3^2}{72} H_6(U) + \dots \right] \quad (3)$$

122 where

123  $U$  = standardized random variable of  $X$

124  $H_k(U)$  = Chebyshev-Hermite polynomials

125  $\phi(U)$  = standard normal density

126  $\kappa_k$  =  $k$ -th order cumulant of  $U$ .

127 Substituting the Edgeworth series into the negentropy definition, Comon (1994) obtained the  
128 analytical expression:

$$129 \quad J(X) = \frac{1}{12} \kappa_3^2 + \frac{1}{48} \kappa_4^2 + \frac{7}{48} \kappa_4^4 - \frac{1}{8} \kappa_3^2 \kappa_4 + O(n^{-2}). \quad (4)$$

130 This is the estimator of negentropy at fourth-order cumulant. In practice, a more intuitive  
131 approximation is commonly used, as follows:

$$132 \quad J(X) = \frac{1}{12} \text{skew}(U)^2 + \frac{1}{48} \text{kurt}(U)^2 \quad (5)$$



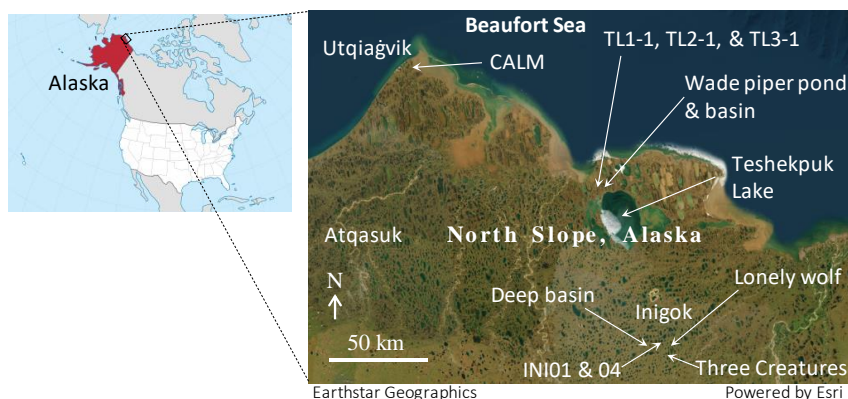
133 where skew and kurt are the skewness and kurtosis of standardized variable,  $U$ , respectively.

134 The sample estimation of the higher-order moment and cumulant (e.g., skew and kurtosis  
135 coefficients) is known to be sensitive to the presence of outliers. In this study, the interquartile  
136 range (IQR) method was adopted for outlier removal with a minimum removal that lies outside  
137 the range of three times IQR.

138 While negentropy metrics and corresponding Edgeworth approximations have been previously  
139 explored and further developed in atmospheric sciences and in physics, including derivations and  
140 implementations to higher-order distributions, elaborate numerical and analytical estimators  
141 (Pires and Perdigão 2007, Perdigão 2010, Perdigão 2017), the present study brings a simplified  
142 treatment not yet explored in Hydrology and tailored for swift and seamless integration within  
143 hydrological and water resource systems investigations.

## 144 2.2 Data collection

145 We analyzed four types of data with different collection methodologies at various scales in this  
146 study. The first is manual snow depth surveys using a GPS-aided snow probe (Magnaprobe;  
147 Sturm & Holmgren, 2018), the second is snow depth transects using a snowmachine-attached  
148 GPR, the third is snow depth maps using UAV-based photogrammetry, and the last is the SWE  
149 product of the ASO. The first three datasets are for the open tundra in the Arctic Coastal Plain  
150 (ACP) of Alaska while the ASO data are for the alpine and subalpine regions of the continental  
151 USA. Detailed data specifications associated with the collection methodologies will be presented  
152 in Results section below. Figure 1 displays the map of the snow depth surveys in North Slope,  
153 Alaska, USA.



154

155

Figure 1: Map of the snow survey locations in Alaska, USA.

## 156 3 Results

### 157 3.1 Manual snow surveys at Teshekpuk, North Slope, Alaska (May 2022)

158 Snow depth data were collected using a Magnaprobe (Sturm & Holmgren, 2018) in five 30 x 30-  
159 m grids with 1 m grid spacing north of Teshekpuk Lake, North Slope, AK, in May 2022. The  
160 GPS location of each measurement was automatically recorded. Figure 2 presents the

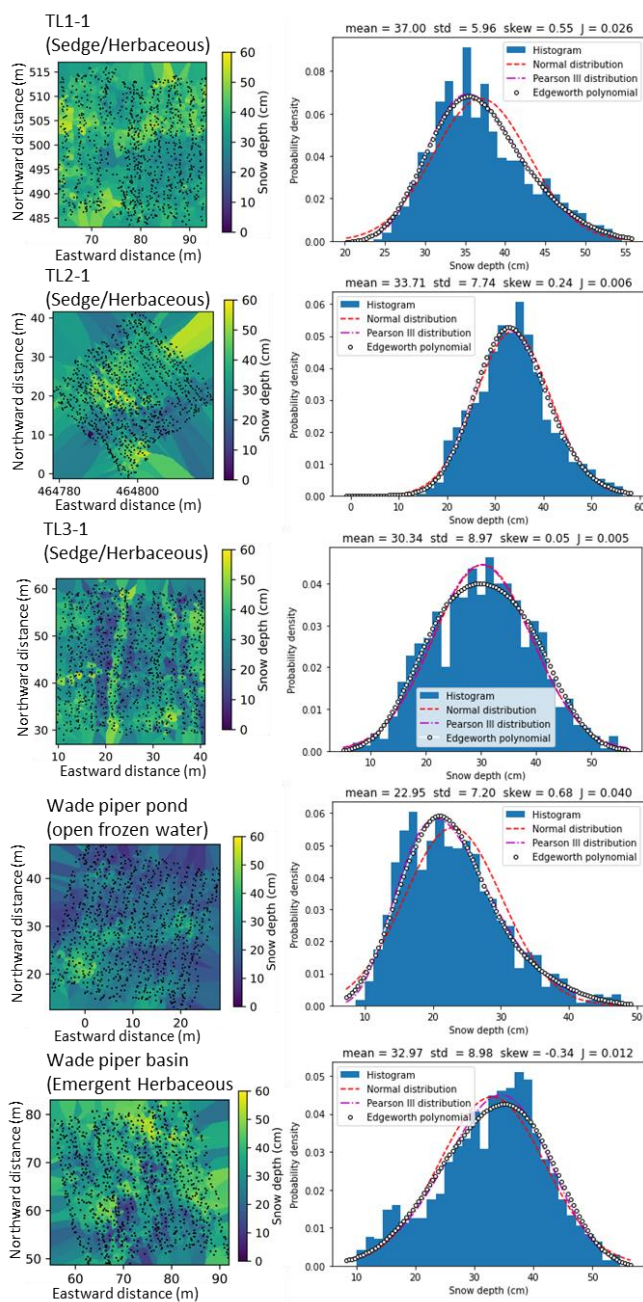


161 interpolated snow depth distributions and corresponding histograms (right columns) in five areas  
162 near Teshekpuk. The observer measured the point scale snow depth at approximately every 1 m  
163 along a line toward flags placed 1 m apart on the surface. Since the data points were selected  
164 from undisturbed snow, the locations are unevenly distributed despite the snowpacks generally  
165 being highly hardened by wind. The relative spatial locations are considered accurate since the  
166 operator stood on the same side of the probe and followed pre-marked lines based on the tape  
167 measure; however, the absolute plotted coordinate in the figures may not be trustworthy due to  
168 the GPS horizontal accuracy  $< 3$  m.

169 The graphics in the left column of Figure 2 present the point depth observation locations and  
170 interpolated snow depth distributions using the nearest distance method. The number of data  
171 points denoted by the black dots is  $n=951$  (TL1-1),  $n=925$  (TL2-1),  $n=904$  (TL3-1),  $n=927$   
172 (Wadepiper Pond), and  $n= 960$  (Wadepiper Basin).

173 The corresponding snow depth histograms and three fitted distributions are displayed in the right  
174 column. The statistics mean, standard deviation, skew coefficient, and negentropy ( $J$ ) are  
175 reported on the top part of each graph. In general, the snow depth distributions in these areas are  
176 almost Gaussian distributions since the computed negentropy is small. However, the negentropy  
177 of snow distribution affected by wind-induced snowdrift (sastrugi) on frozen lakes is larger than  
178 the tundra covered by sedge and herbaceous vegetation. In practice, the non-Gaussianity of  
179 seasonal snow depth may have been negligible in the coastal open tundra (including frozen open  
180 waters) in the Teshekpuk study area in May 2022.





181

182 Figure 2: Manual snow distributions in the Teshekpuk Lake area, North Slope, Alaska (May  
 183 2022) and corresponding histograms with fitted probability density functions (PDFs).  $J$  denotes  
 184 the computed negentropy. Snow depth histograms in open tundra in 30 m x 30 m squares are  
 185 generally categorized as “weak-non-Gaussian.” The approximated center coordinates of the grids



186 are 70.738°N, 153.970°W (TL1-1), 70.740°N, 153.956°W (TL2-1), 70.739°N, 153.928°W (TL3-  
187 1), 70.751°N, 153.870°W (Wadepiper Pond), and 70.746°N, 153.854° W (Wadepiper Basin).

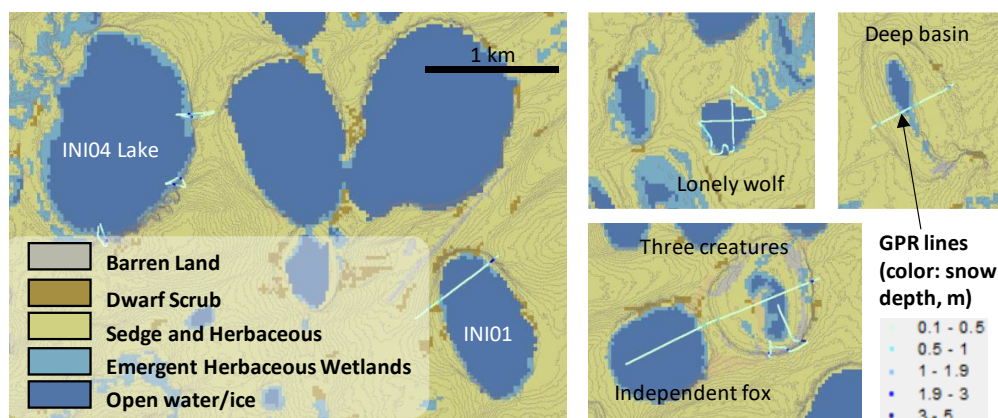
### 188 **3.2 Snow depth surveys using GPR along multiple transects in Inigok, North Slope,** 189 **AK (April 2019)**

190 The Inigok area of North Slope, Alaska (70.001° N, 153.068° W) is characterized by paleo sand  
191 dunes (Carter, 1981), hydro-geomorphological processes, and permafrost landforms such as  
192 thermokarst lake formation and drainage. The landscape is characterized by relatively steep  
193 terrain and substantial wind-induced snowdrifts (deeper than 5 m), especially around lake shores  
194 and drainage channels (e.g., Rangel et al., 2023).

195 Snow depth surveys using a GPR are particularly effective for deep-snow areas since the  
196 Magnaprobe is only 1.5 m long. Considering the lower limit of the selected GPR antenna, we  
197 collected several GPR transects (Malå ProEx, 800 MHz, GuidelineGeo, Sundbyberg, Sweden)  
198 around Inigok, where the snowpack was deeper than in the coastal area. The antenna was placed  
199 on a sled towed by a snowmachine traveling  $< 5\text{ km h}^{-1}$ . The effect of compaction by the  
200 snowmachine was considered negligible because the snow was highly wind-packed and therefore  
201 was not affected by the weight of the snowmachine during data collection. The GPR data were  
202 processed in ReflexW (Sandmeier Software, Karlsruhe, Germany) using a low frequency noise  
203 removal (dewow) and a linear gain with topographic correction adapted from the ArcticDEM  
204 (Rangel et al., 2023b). Maps of snow depth estimated from the GPR transects are shown in  
205 Figure 3. The line color denotes the observed snow depth (the darker, the deeper). A substantial  
206 snowdrift developed near the lakeshore's banks due to its steep topography.

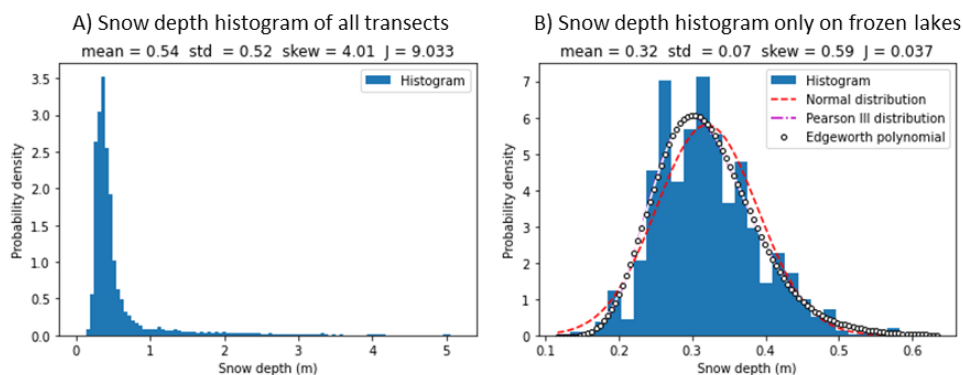
207 Figure 4 displays the histograms of GPR snow depth data in Inigok, North Slope, Alaska, in May  
208 2019 when using (A) all transect data and (B) the frozen lake sections only. The snow depth  
209 histogram of all transects shows strong non-Gaussianity due to a mix of steep and flat terrain.  
210 However, the histogram of the partial dataset only for the frozen lakes shows much weaker non-  
211 Gaussianity. In fact, snow distribution after removing the deep-snow parts can be reasonably  
212 approximated by the Gaussian distribution with a negentropy of 0.037, which is the same level as  
213 Wadepiper Pond (Figure 2) in the previous section ( $J = 0.040$ ). Therefore, the snowdrift due to  
214 steep terrain is considered a major source of non-Gaussianity in snow depth in open tundra.





215

216 Figure 3: Snow depth surveys using GPR along multiple transects in Inigok, North Slope, Alaska  
 217 (27 and 28 April 2019). The approximated center coordinates of the maps are 153.105W  
 218 70.005N (INI04 & INI01), 152.949W 69.993N (Lonely wolf), 153.274W 69.992N (Deep basin),  
 219 and 153.032W 69.942N (Three creatures & Independent fox).



220

221 Figure 4: Snow depth histograms of GPR snow survey data from Inigok, North Slope, Alaska  
 222 (April 2019) using A) all transects and B) sections on frozen lake only. Snow distributions in the  
 223 Inigok area are highly non-Gaussian, while the frozen lake subset shows weak non-Gaussianity.

224

### 225 3.3 Snow depth distribution based on UAV footage of a drained lake basin within 226 the CALM 1-km grid near Utqiagvik, AK (May 2019)

227 Figure 5 (left panel) presents the observed snow distribution of a drained thermokarst lake basin  
 228 referred to as Central Marsh, part of the Circumpolar Active Layer Monitoring (CALM)  
 229 Network located east of Utqiagvik, Alaska. The snow depth was estimated by differentiating the  
 230 snow surface elevation and the snow-free ground elevation using UAV surveys with the  
 231 photogrammetry technique. The images were collected on August 4, 2019 (snow-free), and April  
 232 15, 2019 (snow-covered), using a Phantom 4 UAV (P4RTK). Images were post-  
 233 processed/georeferenced to NAD83 Zone 4 North in ellipsoid heights using a propeller aeropoint

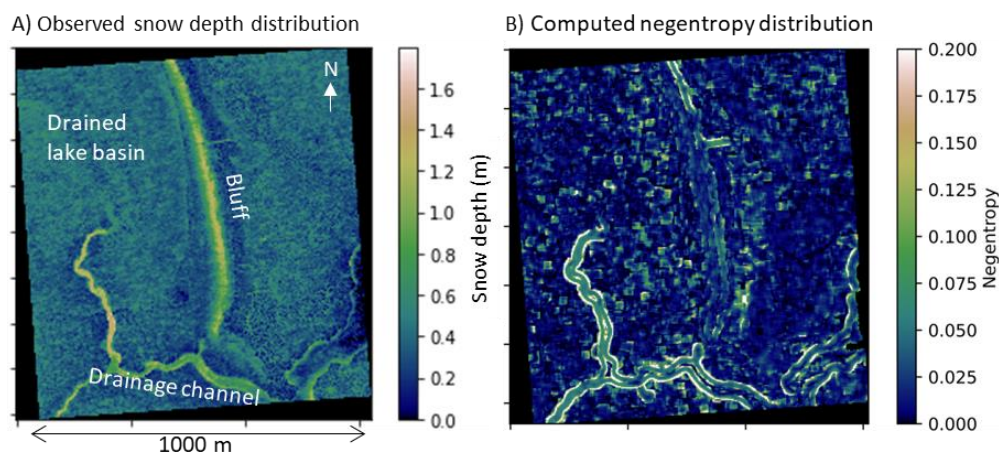


234 and Pix4D (version 4.3.33 for the April survey, 4.4.12 for the August survey) at 0.25 m spatial  
235 resolution (Nichols, 2020). The vertical accuracies of these measurements are 18 cm and 10 cm  
236 for the April and August surveys, respectively. The horizontal resolution for the snow depth is 1  
237 m.

238

239 The CALM site is situated in the ACP in northern Alaska, which has typical complex  
240 terrain due to the recently drained thermokarst lake with sparse or negligible vegetation and well-  
241 developed polygons. There is an obvious smoothed bluff in the center of the domain, and the  
242 west side of this bluff tapers into the drained lake basin. The incised drainage channels cause  
243 steep land features that capture sizable snowdrifts in the southern part. In the southern portion of  
244 the area, the polygons are formed by ground surface cracks with ice wedge development beneath.  
245

246 The negentropy distribution in the moving window may be obtained from this gridded snow data  
247 at a very high spatial resolution. The right panel of Figure 5 presents the computed negentropy  
248 map in the CALM area with a 30-m moving window. Overall, non-Gaussianity in the CALM site  
249 was found to be weak—even with the smoothed bluff and despite high snow depth. However, as  
250 whiter parts in right panel of Figure 5 are found along the drainage channels, topographic  
251 discontinuity around the incised gully seems to cause significant non-Gaussianity. Additionally,  
252 vegetation patches may bring spotty non-Gaussianity in the northern part of the area. Conversely,  
253 since the southern parts covered by the polygons except the drainage channels show darker color  
254 ( $J < 0.025$ ), the ground surface polygon does not make snow distribution non-Gaussian. Overall,  
255 snowpack in the coastal parts of the ACP can reasonably be approximated by Gaussian  
256 distribution since most of the CALM area showed a small negentropy of less than 0.2.



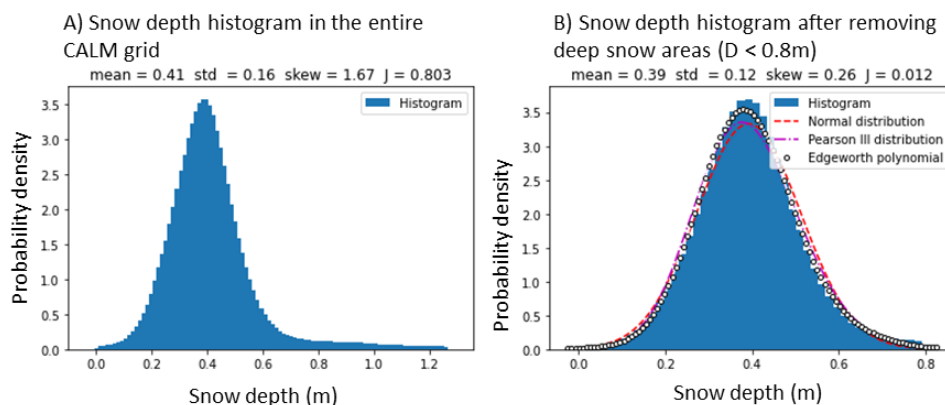
257

258 Figure 5: Snow depth distribution based on UAV photogrammetry and the computed negentropy  
259 distribution of 30-m moving windows in a drained lake basin in the CALM 1-km grid (71.3026°  
260 N, 156.6008°W) near Utqiagvik, Alaska.

261 Figure 6 presents the snow depth histogram, which looks like a Gaussian distribution with a long  
262 tail due to snowdrift around the gullies in the CALM grid. In fact, when the deep snowdrifts of



263 the gully and the bluff are removed from the samples, the histogram more closely resembles a  
 264 Gaussian distribution (see the right panel in Figure 6).



265

266 Figure 6: Snow depth histogram based on the UAV photogrammetry of a drained lake basin in  
 267 the CALM 1-km grid near Utqiagvik, Alaska. Removing the deep snow parts caused by wind-  
 268 induced snowdrift results in a near-perfect fit by Gaussian distribution.

### 269 3.4 SWE products based on ASO data for the selected watersheds

270 SWE is a stable and direct indicator of snow/water distribution in landscapes. As such, the SWE  
 271 products from the Airborne Snow Observatory (ASO) were selected (Painter et al., 2016) to  
 272 examine the Gaussianity of snow distributions in different climate zones and landscapes with  
 273 alpine to subalpine snowpack. The snow depth and SWE distributions were estimated from the  
 274 coupled imaging spectrometer and scanning LiDAR, then combined with distributed snow  
 275 modeling (including snow density simulation). The ASO snow products are considered one of  
 276 the most comprehensive instantaneous snow distribution estimations at fine resolution (50 m).  
 277 We used the processed snow product to characterize the medium-scale snow distribution with the  
 278 same outlier treatment (IQR method) as described above.

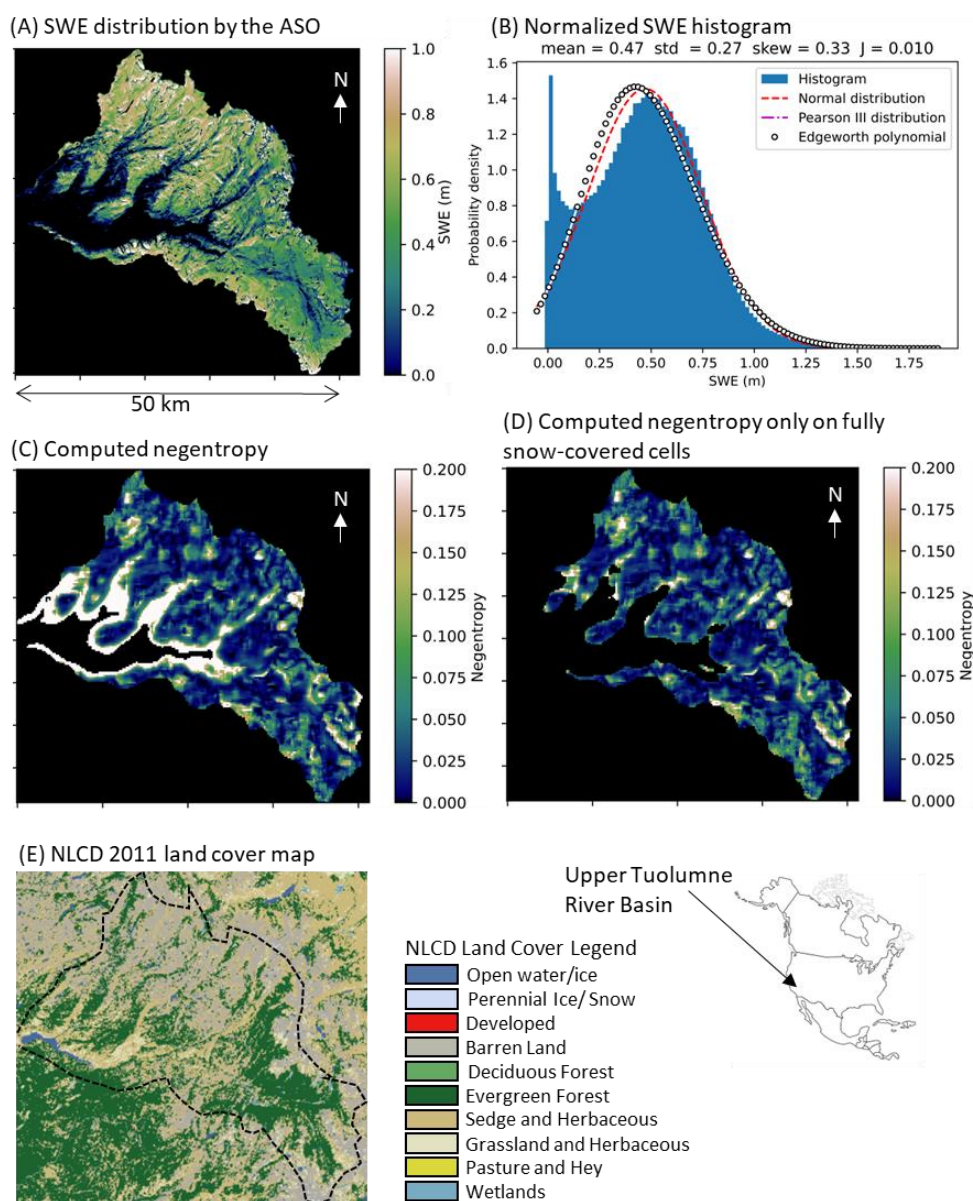
279 The analysis of three representative SWE datasets in the western US is presented. These include  
 280 Upper Tuolumne River watershed in California (USCATB, April 3, 2013), East River watershed  
 281 above Gunnison, Colorado (USCOGE, March 31, 2018), and the Olympic Mountains in  
 282 Washington (USWAOL, March 29, 2016).

#### 283 3.4.1 Tuolumne River Watershed, California

284 Figure 7 presents the composite graphics of the data and the analysis results for the Upper  
 285 Tuolumne River watershed on April 3, 2013. Panel A shows the SWE distribution estimated by  
 286 the ASO, while panel B visualizes the normalized SWE histogram or PDF within the entire  
 287 domain with the fitted theoretical distributions. Panels C and D are the negentropy distributions  
 288 of the SWE within 1500-m moving windows with and without partially snow-covered cells.  
 289 Panel E shows the NLCD 2011 land cover map for reference. The watershed (1175 km<sup>2</sup>) is one  
 290 of the drainages to the California Central Valley through the Hetch Hetchy reservoir in the  
 291 southern Sierra Nevada Mountain Range. The boundary of the catchment is mostly comprised of



292 steep rocky alpine terrain (which contributes to the attractive land features of Yosemite National  
 293 Park), whereas the bottom of the valley is relatively flat due past glacial processes. The snow  
 294 distribution (panel A) shows a clear relationship with elevation, while the SWE barely exceeded  
 295 1 m during the observation period in peak snow season. The overall SWE histogram (panel B)  
 296 illustrates strong non-Gaussianity because of snow-free and shallow accumulation areas in the  
 297 watershed (bounded distribution effect).



298



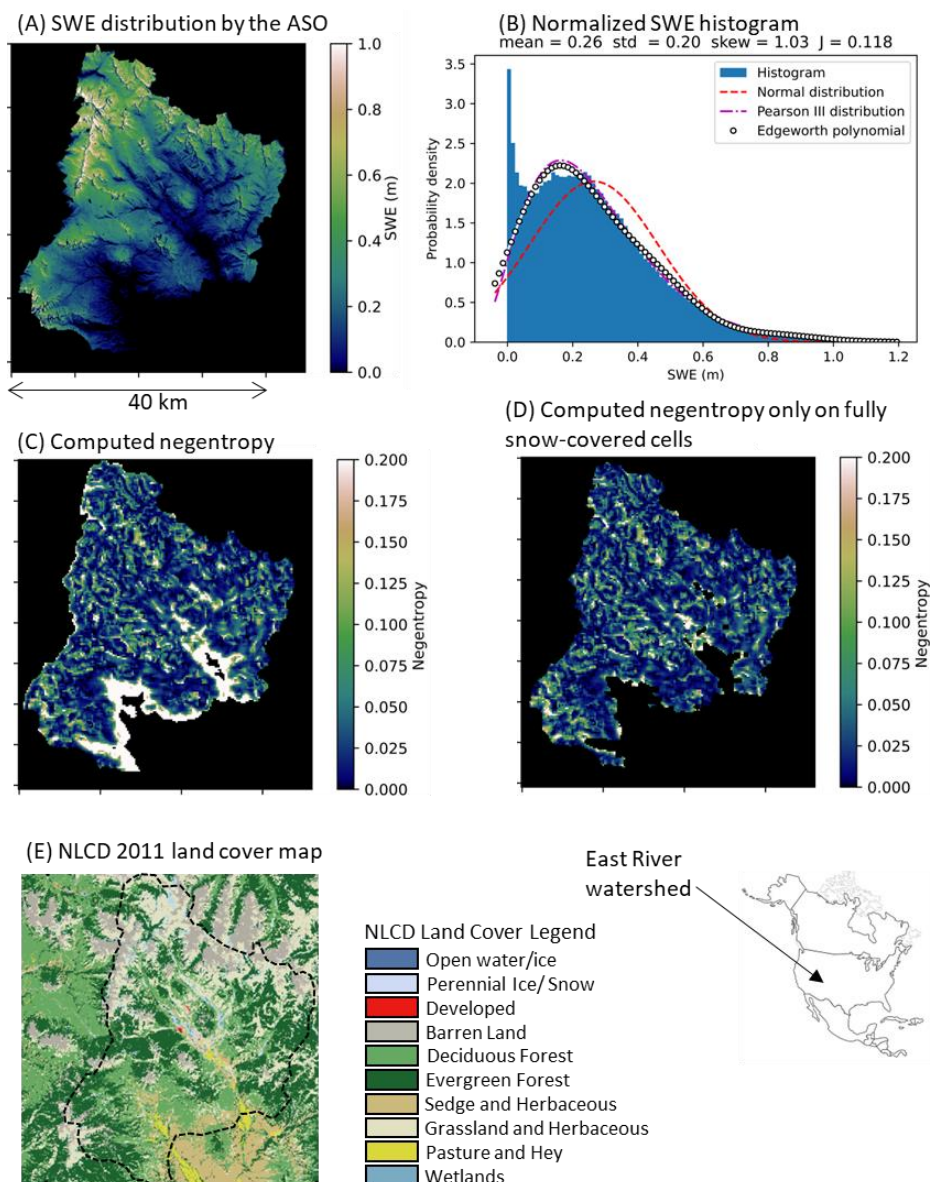


299 Figure 7: (A) SWE distribution based on ASO data of the Upper Tuolumne River Basin,  
300 California, USA from April 3, 2013 (USCATB, 37.461°N, 119.494°W); (B) normalized SWE  
301 histogram; (C) negentropy map of the SWE within 1500-m moving windows; (D) negentropy  
302 map of only fully snow-covered cells; (E) NLCD 2011 land cover map.

303 However, the local negentropy map with moving windows (panel C) shows small non-  
304 Gaussianity except in the low-elevation areas. In fact, the majority of high non-Gaussianity cells  
305 are from partially snow-covered cells. When the partially snow-covered cells are removed in  
306 panel D, the local negentropy falls by less than 0.15 in most of the watershed. Therefore, the  
307 bounded distribution effect in the probability domain from the partially snow-covered cells  
308 brings substantial non-Gaussianity into the snow distribution.

### 309 **3.4.2 East River, Colorado**

310 The ASO dataset of the East River above Gunnison, Colorado (USCOGE) was selected as a  
311 representative basin in the Rocky Mountains region. This dataset includes the U.S. Department  
312 of Energy (DOE)'s East River community observatory, where comprehensive field data have  
313 recently been collected (Kakalia et al., 2020). The data domain, which does not agree with the  
314 watershed boundary, is approximately 1670 km<sup>2</sup> with the elevation ranging from 2,343m  
315 (Gunnison) to 3,901 m. Figure 8 displays the corresponding analysis results of the East River  
316 area on March 31, 2018.



317

318 Figure 8: (A) SWE distribution based on ASO data for the East River watershed above Gunnison,  
 319 Colorado, USA from March 31, 2018 (USCOGE, 39.037°N 106.978°W); (B) normalized SWE  
 320 histogram; (C) negentropy map of the SWE within 1500-m moving windows; (D) negentropy  
 321 map of only fully snow-covered cells; (E) NLCD 2011 land cover map.

322 Besides the obvious bounded distribution effect of partially snow-covered cells, this case study  
 323 illustrates the non-Gaussianity induced by the steep topographic features around the high peaks  
 324 in the Rocky Mountains. Also, since the lower negentropy (darker colored) parts in panel D



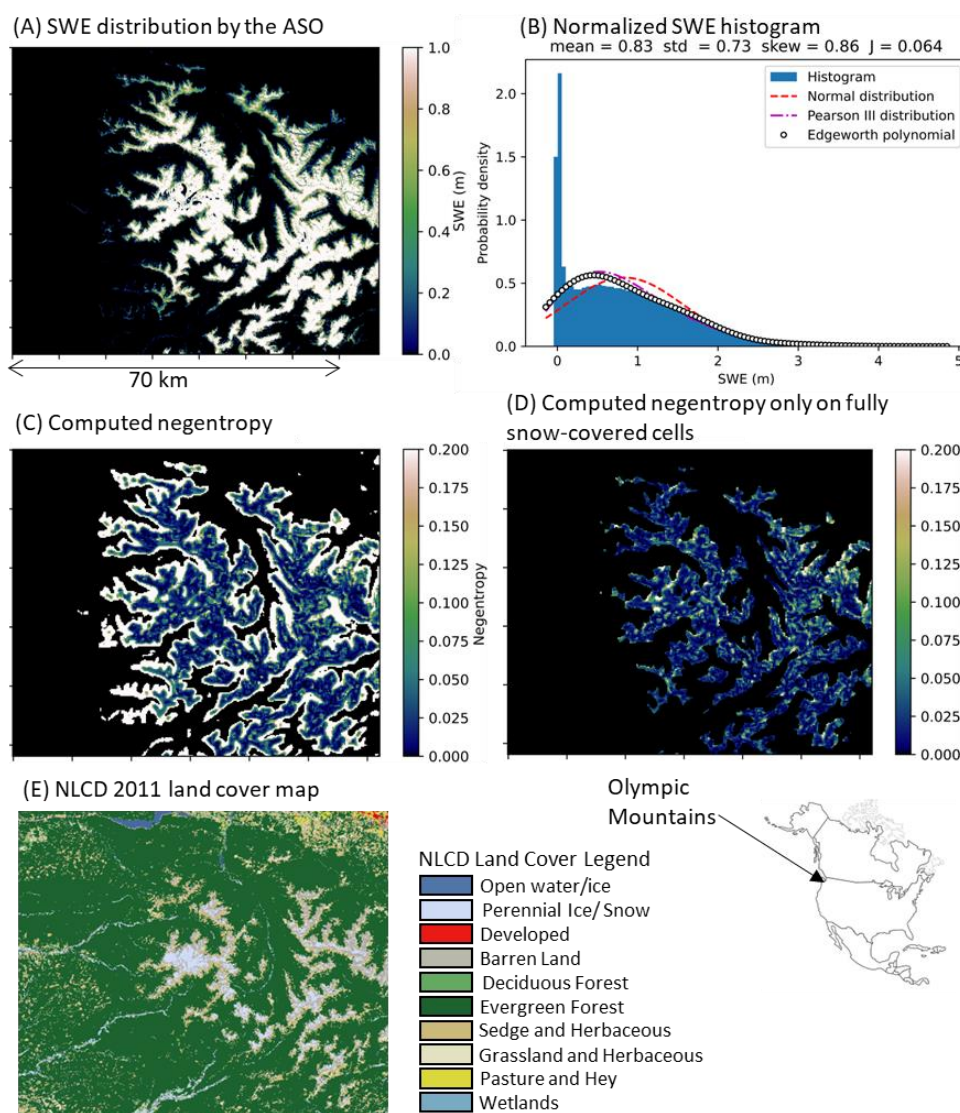


325 generally agree with the evergreen and deciduous forest cover extent in the NLCD land cover  
326 map in panel E, the subalpine forest may reduce non-Gaussianity in snow distribution. However,  
327 the general characteristics of the sample's negentropy distribution in Upper Colorado are  
328 consistent with the Upper Tuolumne River watershed in the Sierra Nevada Mountain Range.



329 **3.4.3 Olympic Mountains, Washington**

330 The last example of snow non-Gaussianity quantification is the Olympic Mountains in  
 331 Washington, USA, which represent the Northern Pacific Coastal Range under strong oceanic  
 332 influence. The elevation ranges from sea level to 2430 m. The Olympic Mountains consist of a  
 333 cluster of steep-sided peaks, heavily forested foothills, and incised deep valleys. The ASO data  
 334 have a large spatial coverage (5,330 km<sup>2</sup>) when compared to the other two ASO datasets  
 335 presented here.



336

337 Figure 9: (A) SWE distribution based on ASO data for the Olympic Mountains, Washington,  
 338 USA from March 29, 2016 (USWAOL, 47.792°N 123.650°W); (B) normalized SWE histogram;



339 (C) negentropy map of the SWE within 1500-m moving windows; (D) negentropy map of only  
340 fully snow-covered cells; (E) NLCD 2011 land cover map.

341 The black areas in the high elevation range in panel A are the approximate glacier extent  
342 excluded from the analysis (Painter et al., 2018). A large fraction of partially snow-covered cells  
343 also introduces non-Gaussianity in SWE in this region. Meanwhile, dense evergreen forests in  
344 the Olympic Mountains seem to effectively reduce the non-Gaussianity of SWE above the snow  
345 line during the ASO scanning period. Overall the non-Gaussianity of the snowpack may be  
346 considered small when compared to the other two examples, which is likely due to denser forest  
347 cover. Presumably, the vegetation cover minimizes the wind-induced snow redistribution process  
348 and makes the snow distribution more Gaussian. These characteristics—i.e., non-Gaussianity in  
349 partially snow-covered areas and high Gaussianity in forested areas—are common features of the  
350 SWE distributions throughout the western US.

#### 351 **4 Discussion**

352 The sample negentropy values presented here are generally consistent with each other despite the  
353 variety of data collection methods used at different scales. The level of random noise in the  
354 datasets depends on the data collection methods. Among the datasets discussed here, one may  
355 anticipate that the ASO data have the largest Gaussian bias due to multiple remote sensing,  
356 resampling, assimilating, and modeling procedures covering remarkable spatial coverages with  
357 uniform data quality. The UAV-based LiDAR data at the North Slope CALM site are expected  
358 to have a noticeable random bias with a vertical accuracy of approximately 12 cm. The GPR  
359 snow depth observations should have a smaller but appreciable Gaussian bias due to snow  
360 quality variation and non-flat snow surface elevation (antenna angle vibration), although the  
361 continuous measurement minimizes the random relative error in the snow depth estimation. The  
362 hand-measured snow depth data using a probe may include the least Gaussian bias, while the  
363 sampling spacing was not uniform and in addition, due to relative poor spatial positioning  
364 control with the Magnaprobe's onboard GPS unit. Despite these differences, it is encouraging  
365 that the quantified Gaussian levels were comparable and consistent since they share common  
366 features.

367 The stability of the sample estimator of negentropy may be a potential issue, especially when the  
368 sample size is small. Additionally, since the higher-order statistical moments are sensitive to the  
369 presence of outliers in the sample, an outlier removal filter is recommended for large samples.  
370 The IQR method with a threshold of 3 IQR above the third quarter (Q3), which is much stricter  
371 than the usual threshold (typically 1.5 IQR), has been applied for the UAV photogrammetry data  
372 and the ASO datasets for computational stability. Even with the large threshold (small outlier  
373 removal), the proposed method using negentropy appears to be effective in characterizing the  
374 Gaussianity of snow distribution, which has been a common implicit assumption for existing  
375 gridded data and models. This study visualized the limitation of such a common distribution  
376 assumption for snow distribution, specifically for areas with partial snow cover.

377 To summarize the analyses presented here, five categories of Gaussianity were defined and  
378 associated with a magnitude of sample negentropy value (see Table 1). Most of the fully snow-



379 covered areas fell into the category “almost Gaussian,” with a negentropy less than 0.03. Notably,  
 380 a negentropy less than 0.01 is considered nearly perfect Gaussian, as can be seen in the previous  
 381 sections.

382 The Gaussianity characterization of snow distribution appears to be useful in distinguishing the  
 383 snowdrift-affected areas using the sample negentropy. Simultaneously, this finding can justify  
 384 the implicit Gaussian assumption for snow distribution for overall SWE estimation, particularly  
 385 for snowpack characterization from remotely sensed information. For instance, the effect of  
 386 higher-order statistical moments can be negligible in most fully snow-covered areas. Conversely,  
 387 some additional statistical treatment for higher order statistics may be required for the areas with  
 388 the non-Gaussian effects around snow lines, open wind-swept areas, and sharp terrains.  
 389 Additionally, since consistent pattern in skew coefficient was not identified from the snow  
 390 datasets, the commonly-used log-normal distribution may not be suitable for those areas.

391 Table 1: Summary of the analysis using the sample negentropy.

Class	Negentropy	Landscape & land cover type	Examples
Strong non-Gaussian	$0.2 < J$	Partially snow-covered areas, mixture of landscapes (steep-flat)	CALM, Inigok, Upper Tuolumne, East River, Olympic Mountains
Non-Gaussian	$0.1 < J \leq 0.2$	Snowdrift around steep terrain	CALM
Weak non-Gaussian	$0.03 < J \leq 0.1$	Snowdrift on a frozen lake, vegetation cluster	Teshkepuk, Inigok, CALM
Nearly Gaussian	$0.01 < J \leq 0.03$	Most of the uniform terrain in open tundra and alpine forest	Teshkepuk, CALM, Upper Tuolumne, East River, Olympic Mountains
Gaussian	$J \leq 0.01$	Open tundra (sedge, polygons), most forested areas	Teshkepuk, Upper Tuolumne, East River, Olympic

392

## 393 5 Conclusions

394 A Gaussian snow distribution is a common underlying assumption for finite scale models or  
 395 gridded datasets. The present study tested this assumption using the sample negentropy of  
 396 various snow data. We found two main sources of non-Gaussianity: (1) partial snow cover effect  
 397 (bounded distribution) and (2) wind-induced snowdrift effect around steep terrain features. The  
 398 second effect may amplify the first one in wind-swept alpine areas since snow erosion remains  
 399 shallow on rocky ridges and peaks. The snowdrift around lakeshore cliffs and deep gullies can  
 400 bring moderate non-Gaussianity in the open tundra of North Slope, Alaska. However, the wind-



401 packed snow in the coastal plain region of the North Slope may generally be categorized as  
402 weakly Gaussian during mid to late winter due to the continuous snow cover. This implies that  
403 the non-Gaussianity of the snowpack may not be neglected during the snow accumulation season  
404 and late spring season. Interestingly, small ground surface features (e.g., low-centered and high-  
405 centered ice wedge polygons) make snow distribution more Gaussian, while snowdrift (snow  
406 dunes) on a flat frozen lake seems to be less Gaussian than on tundra or in a drained lake basin.

407 Our analyses of the ASO SWE products reinforced the findings for snowpacks on the tundra.  
408 Although SWE data was chosen instead of snow depth for practical reasons, the common  
409 features in non-Gaussianity remain valid. Additionally, the snow diffuser effect of forests was  
410 illustrated in three representative areas in the western US. This effect was reported by He et al.  
411 (2019) based on airborne LiDAR snow depth measurements on the Snowy Range, Wyoming,  
412 USA. Hence, it is likely that vegetation cover generally makes snow distribution more Gaussian  
413 in the snow accumulation process; however, further verification of this relationship is  
414 recommended.

415 Overall, a Gaussian distribution is a suitable approximation for snow spatial distribution when  
416 the ground is completely covered by snow. Higher-order statistics associated with landscape type  
417 may potentially improve the SWE estimation in wind-swept open terrain and near snow lines.  
418 The level of non-Gaussianity will determine the choice of statistical tool to correct the systematic  
419 bias in snow measurements. Meanwhile, this study suggests the possibility of partitioning the  
420 extent of wind-induced snowdrifts by means of independent component analysis (Comon et al.,  
421 2010).

## 422 **Author contribution**

423 NO performed the analysis, and RAPP offered technical advice. NO, ADP, RCR, and BMJ  
424 provided the field observed data for the case studies in Alaska. ADP, BMJ, KMH, RAPP, and  
425 RCR actively participated in the discussions and manuscript improvement. NO prepared the  
426 manuscript with contributions from all co-authors.

## 427 **Competing interests**

428 The authors declare that they have no conflict of interest.

## 429 **Acknowledgments**

430 This study was supported by the National Science Foundation (NSF) Office of Polar Programs  
431 (OPP) under the awards 1806287, 1806213, and 1806202. The authors thank UIC Science and  
432 CH2MHill Polar Field Services (now Battelle Arctic Research Operations) for their logistical  
433 field support. RP acknowledges support from the European Union under the Horizon Europe  
434 grant 101074004 (C2IMPRESS), the Meteoceanics flagships MR-220617 and MR-070220-  
435 BLUE. We used the NSIDC DAAC Airborne Snow Observatory (ASO) data downloaded from  
436 NSIDC.org.



## 437 **Data Availability Statement**

438 The data used in this research are publicly available at the NSF Arctic Data Center:

439 <https://doi.org/10.18739/A24746T0K>, and <https://doi.org/10.18739/A2NV99C4P>

440

## 441 **References**

- 442 Aas, K. S., Gislås, K., Westermann, S., & Berntsen, T. K.: A tiling approach to represent  
443 subgrid snow variability in coupled land surface–atmosphere models. *Journal of*  
444 *Hydrometeorology*, 18(1), 49–63, 2017.
- 445 Brubaker, K. L., & Menoes, M. I. C. H. A. E. L.: A technique to estimate snow depletion curves  
446 from time-series data using the beta distribution. In *Proceedings of the Eastern Snow*  
447 *Conference* (Vol. 58, pp. 343–346), 2001.
- 448 Carter, L. D.: A Pleistocene sand sea on the Alaskan Arctic Coastal Plain. *Science*, 211(4480),  
449 381–383. <https://doi.org/10.1126/science.211.4480.381>, 1981.
- 450 Comon, P., & Jutten, C. (Eds.): *Handbook of Blind Source Separation: Independent component*  
451 *analysis and applications*. Academic press, 2010.
- 452 Comon, P., 1994: Independent component analysis, a new concept? *Signal Process.*, 36, 287–314.
- 453 Donald, J. R., Soulis, E. D., Kouwen, N., & Pietroniro, A.: A land cover-based snow cover  
454 representation for distributed hydrologic models. *Water Resources Research*, 31(4), 995–  
455 1009, 1995.
- 456 Egli, L., & Jonas, T.: Hysteretic dynamics of seasonal snow depth distribution in the Swiss  
457 Alps. *Geophysical research letters*, 36(2), 2009.
- 458 Fleming, S. W., Zukiewicz, L., Strobel, M. L., Hofman, H., & Goodbody, A. G.: SNOTEL, the  
459 Soil Climate Analysis Network, and water supply forecasting at the Natural Resources  
460 Conservation Service: Past, present, and future. *JAWRA Journal of the American Water*  
461 *Resources Association*, 2023.
- 462 Hall, D. K., G. A. Riggs, and V. V. Salomonson: MODIS/Terra Snow Cover 5-Min L2 Swath  
463 500m. Version 5. Boulder, Colorado USA: NASA National Snow and Ice Data Center  
464 Distributed Active Archive Center. <http://dx.doi.org/10.5067/ACYTYZB9BEOS>, 2006.
- 465 He, S., Ohara, N., & Miller, S. N.: Understanding subgrid variability of snow depth at 1-km scale  
466 using Lidar measurements. *Hydrological Processes*, 33(11), 1525–1537, 2019.
- 467 He, S., Smirnova, T. G., & Benjamin, S. G.: Single-Column Validation of a Snow Subgrid  
468 Parameterization in the Rapid Update Cycle Land-Surface Model (RUC LSM). *Water*  
469 *Resources Research*, 57(8), e2021WR029955, 2021.





- 470 Hyvärinen, A., Karhunen, J., & Oja, E.: Independent component analysis and blind source  
471 separation. ISBN:9780471221319, |DOI:10.1002/0471221317, John Wiley & Sons, Inc.,  
472 2001.
- 473 Kakalia, Z., Varadharajan, C., Alper, E., Brodie, E., Burrus, M., Carroll, R., ... & Agarwal, D.:  
474 The East River Community Observatory Data Collection: Diverse, multiscale data from  
475 a mountainous watershed in the East River, Colorado. *Authorea Preprints*, 2020.
- 476 Kolberg, S. A., & Gottschalk, L.: Updating of snow depletion curve with remote sensing  
477 data. *Hydrological Processes: An International Journal*, 20(11), 2363-2380, 2006.
- 478 Liston, G. E.: Representing subgrid snow cover heterogeneities in regional and global  
479 models. *Journal of climate*, 17(6), 1381-1397, 2004.
- 480 Luce, C. H., & Tarboton, D. G.: The application of depletion curves for parameterization of  
481 subgrid variability of snow. *Hydrological processes*, 18(8), 1409-1422, 2004.
- 482 Luce, C. H., Tarboton, D. G., & Cooley, K. R.: Sub-grid parameterization of snow distribution  
483 for an energy and mass balance snow cover model. *Hydrological Processes*, 13(12-13),  
484 1921-1933, 1999.
- 485 Meloche, J., Langlois, A., Rutter, N., Royer, A., King, J., Walker, B., ... & Wilcox, E. J.:  
486 Characterizing tundra snow sub-pixel variability to improve brightness temperature  
487 estimation in satellite SWE retrievals. *The Cryosphere*, 16(1), 87-101, 2022.
- 488 Meng, C.: Quantifying the impacts of snow on surface energy balance through assimilating snow  
489 cover fraction and snow depth. *Meteorology and Atmospheric Physics*, 129, 529-538,  
490 2017.
- 491 Mott, R., Daniels, M., & Lehning, M.: Atmospheric flow development and associated changes in  
492 turbulent sensible heat flux over a patchy mountain snow cover. *Journal of*  
493 *Hydrometeorology*, 16(3), 1315-1340, 2015.
- 494 Mott, R., Schlögl, S., Dirks, L., & Lehning, M.: Impact of extreme land surface heterogeneity on  
495 micrometeorology over spring snow cover. *Journal of Hydrometeorology*, 18(10), 2705-  
496 2722, 2017.
- 497 Nichols, I.O.: Assessing the accuracy of a UAV snow depth survey Utqiagvik (Barrow), Alaska  
498 calm grid, M. S. Thesis, Geological Engineering, Michigan Technological University,  
499 2020.
- 500 Nitta, T., Yoshimura, K., Takata, K., O'ishi, R., Sueyoshi, T., Kanae, S., ... & Liston, G. E.:  
501 Representing variability in subgrid snow cover and snow depth in a global land model:  
502 offline validation. *Journal of climate*, 27(9), 3318-3330, 2014.
- 503 Painter, T. H., Berisford, D. F., Boardman, J. W., Bormann, K. J., Deems, J. S., Gehrke, F., ... &  
504 Winstral, A.: The Airborne Snow Observatory: Fusion of scanning lidar, imaging  
505 spectrometer, and physically-based modeling for mapping snow water equivalent and  
506 snow albedo. *Remote Sensing of Environment*, 184, 139-152, 2016.



- 507 Painter, Thomas H. and Dennis P. Lettenmaier: GPM Ground Validation Airborne Snow  
508 Observatory (ASO) OLYMPEX [indicate subset used]. Dataset available online from  
509 the NASA Global Hydrometeorology Resource Center DAAC, Huntsville, Alabama,  
510 U.S.A. DOI: <http://dx.doi.org/10.5067/GPMGV/OLYMPEX/LIDAR/DATA101>, 2018.
- 511 Pires, C.A., and R.A.P. Perdigão: Non-Gaussianity and Asymmetry of the Winter Monthly  
512 Precipitation Estimation from the NAO. *Mon. Wea. Rev.*, 135, 430–448,  
513 <https://doi.org/10.1175/MWR3407.1>, 2007.
- 514 Perdigão, R.A.P.: Nonlinear statistics and dynamics of atmospheric predictability and  
515 downscaling. <http://hdl.handle.net/10451/2013>, 2010.
- 516 Perdigão, R.A.P.: Fluid Dynamical Systems: From Quantum Gravitation to Thermodynamic  
517 Cosmology. <https://doi.org/10.46337/mdsc.5091>, 2017.
- 518 Perdigão, R.A.P.: Polyadic Entropy, Synergy and Redundancy among Statistically Independent  
519 Processes in Nonlinear Statistical Physics with Microphysical Codependence. *Entropy*  
520 2018, 20, 26. <https://doi.org/10.3390/e20010026>, 2018.
- 521 Rangel, R. C., Ohara, N., Parsekian, A. D., and Jones, B. M.: Arctic Tundra Lake Drainage  
522 Increases Snow Storage in Drifts. *Journal of Geophysical Research: Earth Surface*,  
523 e2023JF007294, 2023a.
- 524 Rangel, R. C., Parsekian, A. D., Ohara, N., and Jones, B. M.: Ground Penetrating Radar (GPR)  
525 data on snow over lakes and drained lake basins in Inigok, North Slope of Alaska, April  
526 2019. Arctic Data Center. doi:10.18739/A2NV99C4P, 2023b.
- 527 Santanello Jr, J. A., Dirmeyer, P. A., Ferguson, C. R., Findell, K. L., Tawfik, A. B., Berg, A., ...  
528 & Wulfmeyer, V.: Land–atmosphere interactions: The LoCo perspective. *Bulletin of the*  
529 *American Meteorological Society*, 99(6), 1253-1272, 2018.
- 530 Sengupta, A., Singh, B., DeFlorio, M. J., Raymond, C., Robertson, A. W., Zeng, X., ... & Jones,  
531 J.: Advances in subseasonal to seasonal prediction relevant to water management in the  
532 western United States. *Bulletin of the American Meteorological Society*, 103(10),  
533 E2168-E2175, 2022.
- 534 Shamir, E., & Georgakakos, K. P.: Estimating snow depletion curves for American River basins  
535 using distributed snow modeling. *Journal of Hydrology*, 334(1-2), 162-173, 2007.
- 536 Skaugen, T., & Randen, F.: Modeling the spatial distribution of snow water equivalent, taking  
537 into account changes in snow-covered area. *Annals of Glaciology*, 54(62), 305-313,  
538 2013.
- 539 Sturm, M., & Holmgren, J.: An automatic snow depth probe for field validation campaigns.  
540 *Water Resources Research*, 54(11), 9695-9701, 2018.
- 541 Tarricone, J., Webb, R. W., Marshall, H. P., Nolin, A. W., & Meyer, F. J.: Estimating snow  
542 accumulation and ablation with L-band interferometric synthetic aperture radar  
543 (InSAR). *The Cryosphere*, 17(5), 1997-2019, 2023.



- 544 Tsang, L., Durand, M., Derksen, C., Barros, A. P., Kang, D. H., Lievens, H., ... & Xu, X.: Global  
545 monitoring of snow water equivalent using high-frequency radar remote sensing. *The*  
546 *Cryosphere*, 16(9), 3531-3573, 2022.
- 547 Younas, W., Hay, R. W., MacDonald, M. K., ul ISLAM, S., & Dery, S. J.: A strategy to  
548 represent impacts of subgrid-scale topography on snow evolution in the Canadian Land  
549 Surface Scheme. *Annals of Glaciology*, 58(75pt1), 1-10, 2017.